The dynamics of vortex streets in channels

Xiaolin Wang and Silas Alben

Citation: Physics of Fluids **27**, 073603 (2015); doi: 10.1063/1.4927462
View online: http://dx.doi.org/10.1063/1.4927462
View Table of Contents: http://scitation.aip.org/content/aip/journal/pof2/27/7?ver=pdfcov
Published by the AIP Publishing

PHYSICS OF FLUIDS **27**, 073603 (2015)

The dynamics of vortex streets in channels

Xiaolin Wang[1,2,a)] and Silas Alben[1,a)]
[1]*Department of Mathematics, University of Michigan, Ann Arbor, Michigan 48109, USA*
[2]*Department of Mathematics, Georgia Institute of Technology, Atlanta, Georgia 30332, USA*

(Received 17 December 2014; accepted 15 July 2015; published online 31 July 2015)

We develop a model to numerically study the dynamics of vortex streets in channel flows. Previous work has studied the vortex wakes of specific vortex generators. Here, we study a wide range of vortex wakes including regular and reverse von Kármán streets with various strengths, geometries, and Reynolds numbers (Re) by applying a smoothed von Kármán street as an inflow condition. We find that the spatial structure of the inflow vortex street is maintained for the reverse von Kármán street and altered for the regular street. For regular streets, we identify a transition to asymmetric dynamics which happens when Re increases, or vortices are stronger, or vortex streets are compressed horizontally or extended vertically. We also determine the effects of these parameters on vortex street inversion.
[http://dx.doi.org/10.1063/1.4927462]

I. INTRODUCTION

In recent years, vorticity-enhanced heat transfer has become an important research topic due to the faster heat transfer requirement for increased processing power of compact electronic devices.[1–6] The problem involves fundamental issues in both fluid dynamics and heat transfer. In this work, we investigate vortex dynamics in channel flows, commonly used in the convection cooling.

In channel flows, bluff bodies and vibrating plates have been employed to generate vortices to improve mixing. Much previous work has been conducted on their resulting vortex wakes. For example, von Kármán's inviscid point vortex street approximates the wake structure of a bluff body by a staggered array of oppositely signed vortices[7] and has been used to represent vortex shedding by different body shapes including circular and square cylinders[8,9] and inclined flat plates.[10] Among the topics of study on vortex shedding are the formation of vortex wakes,[11–13] shear layer instabilities,[14,15] and numerical simulation methods.[6,16]

Another type of vortex generator induces vortices using an oscillating plate. Depending on the rigidity of the plate, the Reynolds number, and the amplitude and the frequency of the oscillation, the plate can generate distinct vortex wakes at its trailing edge including regular and reverse von Kármán streets and more complicated patterns.[17] Schnipper *et al*. showed six different vortex wake structures obtained by pitching oscillations of a foil in a vertically flowing soap film for different Strouhal numbers and pitching amplitudes.[18] Godoy-Diana *et al*. obtained a similar phase diagram which shows transitions between different vortex wake structures.[19] Among these different vortex wakes, perhaps the simplest are the regular and the reverse von Kármán streets. The former is analogous to the vortex wake behind a bluff body and can also be obtained by passive flapping of a flexible flag.[20–22] This phenomenon was experimentally examined by Taneda[23] and Zhang *et al*.[24] using gravity-driven soap-film tunnels. Alben and Shelley[25] and Michelin *et al*.[26] studied the regime in which the motion of the flag is periodic and a von Kármán street is shed from the trailing edge of the flag. Their models used different inviscid flow descriptions, but their results are in good agreement with respect to the positions of the shed vortices' centers. Under proper conditions,[27] a vibrating plate can also create a reverse von Kármán street at the trailing edge. This type of vibration has drawn attention from the

[a)]Electronic addresses: wxiaolin@umich.edu and alben@umich.edu

biolocomotion community, as a flapping foil can model the generation of locomotor and maneuvering forces in the flying and swimming of animals.[28–30]

Although many studies have been conducted on this subject, several aspects of the problem require further investigation. Most of the previous work on the vortex wake focuses either on the formation mechanism of the shed vortices or on the development of the flow in an unbounded region. There are fewer studies of the development of the von Kármán street in a bounded channel[31–37] and even fewer results for the reverse von Kármán street.[5,38] Davis *et al.*[31] carried out a numerical and experimental study of the confined flow around rectangular cylinders for two different blockage ratios and a wide range of *Re* and found increased drag and Strouhal number due to the presence of the channel walls. Suzuki *et al*.[32] studied the flow in a channel obstructed by a square rod and gave special attention to the crossing of the upper and lower rows of the vortex street. They found the main cause that the vortex street's inversion was the coupling of the wake vorticity and the separated boundary layer from the wall. Camarri and Giannetti further investigated the inversion of the vortex street in the wake of a confined square cylinder.[33] They proposed that for low to moderate blockage ratios, this phenomenon depends on the amount of vorticity in the incoming upstream flow, which was confirmed through simulations with artificial inflow conditions to control the vorticity introduced into the flow. Singha and Sinhamahapatra[34] focused on the confined flow dynamics with a circular cylinder as the obstacle at Reynolds number less than 250 and found that the transition from steady flow to periodic vortex shedding is delayed due to the wall confinement. Zovatto and Pedrizzetti[35] studied the vortex wake pattern of a cylinder placed asymmetrically in the channel and showed that the vortex wake changes to a single row of same-sign vortices as the body approaches one wall. Similar studies were also carried out on vibrating plates. Guo and Paidoussis[36] studied the stability of a rectangular plate in inviscid channel flow with different boundary conditions at the leading and trailing edges. Alben[37] considered a similar problem of a flapping flag in an inviscid channel with a vortex sheet model. Gerty[5] and Hidalgo and Glezer[38] experimentally investigated the flow induced by a vibrating reed in a channel which includes a reverse von Kármán street.

Most previous work only focused on a specific type of vortex generator, since the flow past a vibrating plate and a bluff body are quite different. Therefore, comparisons between different vortex generators are difficult. In this work, we propose a model to simulate the fluid dynamics of a wide range of vortex generators in channel flow by approximating the vortex shedding with modified regular and reverse von Kármán streets. We then apply the model to vortex streets with various strengths and geometries and discuss how the wall confinement affects the vortex dynamics.

The paper is organized as follows: Sec. II describes the model for the vortex dynamics, Sec. III discusses the numerical method for solving the model, Sec. IV studies the effects of fluid parameters on vortex dynamics, and the conclusions follow in Sec. V.

II. MODELLING

We model the fluid dynamics of a two-dimensional viscous flow in a channel. The channel has length L and height H, and the fluid has kinematic viscosity ν. A background flow is present in the channel, and for simplicity, we only consider the case of a uniform flow U_b. The flow satisfies the two-dimensional incompressible Navier-Stokes equations in vorticity-stream function form,

$$\frac{\partial \omega}{\partial t} + \mathbf{u} \cdot \nabla \omega = \nu \Delta \omega, \tag{1}$$

$$-\Delta \psi = \omega. \tag{2}$$

Here, $\omega(x, y, t)$ and $\psi(x, y, t)$ denote the vorticity and the stream function of the flow, respectively. The velocity $\mathbf{u} = (u, v)$ is obtained from the stream function by

$$u(x, y) = \frac{\partial \psi}{\partial y}, \quad v(x, y) = -\frac{\partial \psi}{\partial x}. \tag{3}$$

A schematic figure of the computational domain is shown in Figure 1.

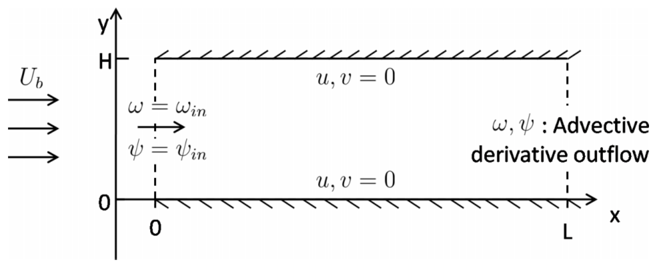

FIG. 1. Schematic of the computational domain with a uniform background flow U_b. The channel has length L and height H. Dirichlet boundary conditions are applied at the entrance of the channel. No-penetration and no-slip conditions are used at the walls and advective derivative conditions are applied to both ω and ψ at the outflow.

A. Boundary conditions

To solve the Navier-Stokes equations, we need to impose proper boundary conditions for ω and ψ on each boundary. We discretize the channel with an $N \times M$ uniform spatial grid which has N points in the x direction and M points in the y direction. The indices $(1,1),(N,1),(M,N)$, and $(1,M)$ indicate the lower left, lower right, upper right, and upper left corners of the computational domain, respectively.

No-slip ($u = 0$) and no-penetration ($v = 0$) conditions are applied at the upper and lower wall boundaries of the channel. Both conditions involve ψ, while neither involves the vorticity ω. To obtain a boundary condition for ω, Briley[39] proposed a fourth-order formula for the vorticity boundary values by using the near-boundary stream function values,

$$\omega_{i,1} = \frac{1}{18h^2}(85\psi_{i,1} - 108\psi_{i,2} + 27\psi_{i,3} - 4\psi_{i,4}) \equiv \omega^B_{i,1}, \quad \forall i = 1,2,\ldots,N, \tag{4}$$

$$\omega_{i,M} = \frac{1}{18h^2}(85\psi_{i,M} - 108\psi_{i,M-1} + 27\psi_{i,M-2} - 4\psi_{i,M-3}) \equiv \omega^B_{i,M}, \quad \forall i = 1,2,\ldots,N. \tag{5}$$

Here, $h = 1/(M-1)$ denotes the grid spacing in the y direction. Briley's formula is obtained by discretizing the no-slip condition $\partial\psi/\partial y = 0$ with a fourth-order finite difference approximation and then applying it to Equation (2). The advantage of using a fourth-order instead of a second-order formula on wall boundaries was discussed by Napolitano[40] as he reported smaller global errors in two numerical examples when using a high-order scheme. The no-penetration condition $\partial\psi/\partial x = 0$ gives a Dirichlet boundary condition for ψ,

$$\psi_{i,1} = \psi_{1,1}, \quad \psi_{i,M} = \psi_{1,M}, \quad i = 1,2,\ldots,N, \tag{6}$$

where $\psi_{1,1}$ and $\psi_{1,M}$ are the values of ψ at the inflow boundaries, to be given later.

Outflow boundary conditions are used to approximate conditions at the channel exit. If the flow is laminar and the channel is sufficiently long, the flow approaches a Poiseuille flow at the exit, in which case the natural boundary condition is a reasonable choice,[41,42]

$$\partial_n\omega = 0, \quad \partial_n\psi = 0, \tag{7}$$

where n is the outward normal coordinate at the exit. This implies that the vertical velocity is zero at the exit, which is true for Poiseuille flow. However, when the channel is not very long, the flow can still be transient at the exit, and conditions based on unsteady problems are required. Much previous work has been carried out on the proper outflow conditions in this case.[42–45] In this work, we apply the advective derivative condition[46–48] for ω and ψ at the outflow boundary. Sani and Gresho[48] proposed this condition for the velocity variables,

$$\frac{\partial \mathbf{u}}{\partial t} + c\frac{\partial \mathbf{u}}{\partial n} = 0, \tag{8}$$

where c is an average outflow velocity (for example, the averaged streamwise velocity across the exit, $\bar{u}$[48]). Later, Comini and Manzan[47] derived conditions for ω and ψ based on Equation (8),

$$\frac{\partial \omega}{\partial t} + \bar{u}\frac{\partial \omega}{\partial n} = 0, \tag{9}$$

$$\frac{\partial}{\partial t}\left(\frac{\partial \psi}{\partial x}\right) + \bar{u}\left(-\frac{\partial^2 \psi}{\partial y^2} - \omega\right) = 0. \tag{10}$$

Equation (10) is numerically solvable at the exit by combining the wall values of ψ, from the prescribed inflow (discussed next), with the no-penetration condition. The advantage of this condition is that the numerical error caused by truncating the finite domain only affects a local region close to the exit and does not cause flow disturbances further upstream.[48] In this work, we choose $L = 4H$ for the simulations. This is a moderate length which allows enough flow development without excessive computational cost.

Finally, we discuss the inflow boundary conditions. We want to approximate situations where a vortex generator is placed in front of the channel so that vortices are created and driven into the channel by an imposed background flow. We model the wakes of such vortex generators as modified reverse or regular von Kármán vortex streets with various geometries and strengths.

In inviscid flow, the complex potential of a von Kármán point vortex street is[7,49]

$$w_{vk} = \phi_{vk} + i\psi_{vk} = \frac{i\Gamma}{2\pi}\log\left(\sin\frac{\pi}{a}(z - z_0)\right) - \frac{i\Gamma}{2\pi}\log\left(\sin\frac{\pi}{a}\left(z - z_0 - \frac{1}{2}a - ib\right)\right), \tag{11}$$

and the corresponding complex velocity is

$$\mathbf{u}_{vk} = u(z) - iv(z) = \frac{i\Gamma}{2a}\cot\left(\frac{\pi}{a}(z - z_0)\right) - \frac{i\Gamma}{2a}\cot\left(\frac{\pi}{a}\left(z - z_0 - \frac{1}{2}a - ib\right)\right), \tag{12}$$

where point vortices with strength Γ are placed at $z_0 + (m + \frac{1}{2})a + ib$ and those with strength $-\Gamma$ are placed at $z_0 + ma, m = 0, \pm 1, \pm 2, \ldots$. Positive Γ gives a reverse von Kármán street, while negative Γ gives a regular von Kármán street. Equation (12) has a singularity $\sim 1/z$ at the point vortex location. However, the point vortex itself travels with a finite velocity because it does not induce velocity at its own location.[7,49] The velocity at $z = z_0$ is

$$U_p = \frac{\Gamma}{2a}\tanh\frac{\pi b}{a}. \tag{13}$$

By symmetry, each vortex moves with the same velocity U_p.

To obtain a more realistic inflow at moderate Reynolds number, we replace the point vortices in Equation (12) by finite-size vortices, or "vortex blobs," to account for viscous diffusion. The blob has radius δ, and the velocity inside the blob is computed by subtracting the point-vortex singularity from the von Kármán street solution and adding a desingularized kernel. The complex velocity, the stream function, and the vorticity inside the mth blob are defined as

$$\mathbf{u}_{blob} = \mathbf{u}_{vk}(z) - \frac{i\Gamma}{2\pi}\frac{1}{z - z_m} + \frac{i\Gamma}{2\pi}\frac{\bar{z} - \bar{z}_m}{|z - z_m|^2 + \delta^2}, \tag{14}$$

$$\psi_{blob} = \psi_{vk} + \frac{\Gamma}{2\pi}\log(|z - z_m|) - \frac{\Gamma}{2\pi}\log(\sqrt{|z - z_m|^2 + \delta^2}), \tag{15}$$

$$\omega_{blob} = \frac{\Gamma\delta^2}{\pi(|z - z_m|^2 + \delta^2)^2}. \tag{16}$$

Here, the subscript "vk" denotes the von Kármán street solution, and z_m is the location of the mth blob. The δ-term is an artificial smoothing kernel that regularizes the point vortex. It is analogous to the desingularized kernel used by Krasny,[50] and as $\delta \to 0$, the velocity tends to that of a point vortex model. In the region 2δ away from the vortex blob center, we use the velocity of the unmodified point vortex von Kármán street. A cubic Hermite interpolation (denoted by subscript "herm") is used to obtain a smooth transition between the two different velocity fields,

$$u(z) - iv(z) = \begin{cases} \mathbf{u}_{vk}(z), & |z - z_m| > 2\delta, \\ \mathbf{u}_{herm}, & \delta < |z - z_m| \le 2\delta, \\ \mathbf{u}_{blob}, & 0 < |z - z_m| \le \delta. \end{cases} \tag{17}$$

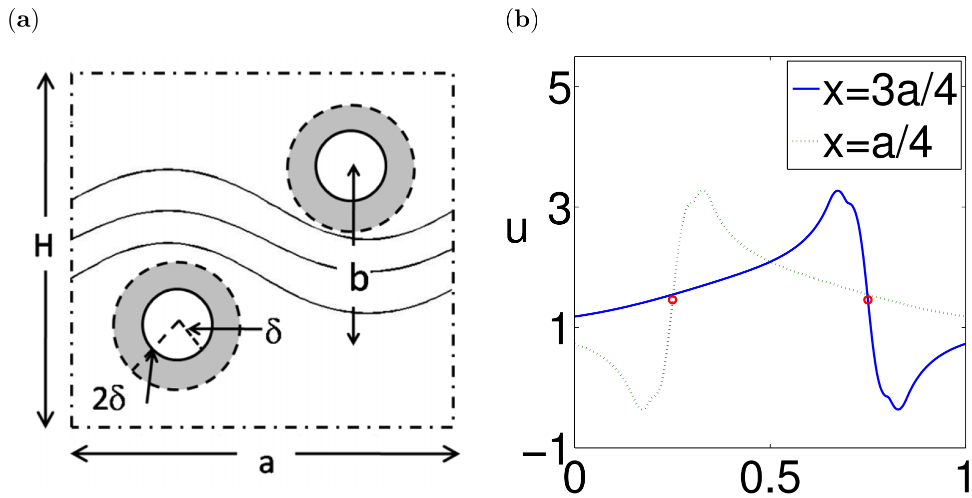

FIG. 2. (a) A schematic figure of the vortex blob model. The horizontal and vertical displacements between adjacent blobs are $\frac{1}{2}a$ and b, respectively. The blobs have radii δ and are located at $z = \frac{1}{4}a + i\frac{1}{2}(H-b)$ and $z = \frac{3}{4}a + i\frac{1}{2}(H+b)$; (b) cross-sectional values of u at $x = \frac{1}{4}a$ and $x = \frac{3}{4}a$, with $U_b = 1$, $\Gamma = 1$, and $\delta = 0.05$. The circles indicate the centers of the vortex blobs.

The vortex blobs move with the same velocity as in the point vortex case since the blob does not contribute to its own velocity and the contributions of all the other blobs are the same as in the point vortex model as they are more than 2δ away. Thus, the vortex blob with an additional uniform background flow U_b has speed

$$U = U_b + \frac{\Gamma}{2a}\tanh\frac{\pi b}{a}. \tag{18}$$

A schematic figure of the vortex blob model and values of the horizontal velocity u on cross sections through the blob centers for $U_b = 1, \Gamma = 1, a/H = 1$, and $b/H = 0.5$ are shown in Figures 2(a) and 2(b), respectively.

The inflow just described is periodic in x (with period a) and time (with period $\tau_p = a/U$). It is a good approximation of the formation of the vortex street when the vorticity has only diffused slightly. In the numerical simulation, we pre-compute the values of the velocities, vorticity, and stream function over one period at the upstream boundary, and then at each time instant t, we impose the appropriate values at t as $\omega = \omega_{in}, \psi = \psi_{in}, u = u_{in}$, and $v = v_{in}$.

We summarize all the boundary conditions for fluid Equations (1) and (2),

$$\omega = \omega_{in}, \quad \psi = \psi_{in}, \qquad x = 0, 0 < y < H, \tag{19}$$

$$\frac{\partial\omega}{\partial t} + \bar{u}\frac{\partial\omega}{\partial x} = 0, \quad \frac{\partial}{\partial t}\left(\frac{\partial\psi}{\partial x}\right) + \bar{u}\left(-\frac{\partial^2\psi}{\partial y^2} - \omega\right) = 0, \qquad x = L, 0 < y < H, \tag{20}$$

$$\omega = \omega_1^B, \quad \psi = \psi_{1,1}, \qquad 0 \le x \le L, y = 0, \tag{21}$$

$$\omega = \omega_M^B, \quad \psi = \psi_{1,M}, \qquad 0 \le x \le L, y = H, \tag{22}$$

where $\psi_{1,1}$ and $\psi_{1,M}$ are obtained from ψ_{in}.

B. Nondimensionalization

We classify our flows as either vortex-dominated or background-flow-dominated based on the incoming vortex street conditions. When the strength of the vortex blob $|\Gamma|$ is larger than the background flow $|U_b H|$, we define the flow as vortex-dominated. Otherwise, the flow is background-flow-dominated. This criterion is applied for both the reverse and regular von Kármán streets.

For simplicity, we use the original notation to indicate all the dimensionless variables. Then, Equations (1)–(3) become

$$\frac{\partial \omega}{\partial t} + \mathbf{u} \cdot \nabla \omega = \frac{1}{Re} \Delta \omega, \tag{23}$$

$$-\Delta \psi = \omega, \tag{24}$$

$$u = \frac{\partial \psi}{\partial y}, \quad v = -\frac{\partial \psi}{\partial x}, \tag{25}$$

with several important dimensionless parameters:

1. $S_b = \dfrac{b}{H}$, the dimensionless vertical distance between the two rows of vortices.
2. $S_a = \dfrac{a}{H}$, the dimensionless horizontal period length.

For the vortex-dominated regime, we choose $|\Gamma|/H$ as the characteristic velocity, and the dimensionless parameters also include:

3. $Re = \dfrac{|\Gamma|}{\nu}$, the Reynolds number.
4. $U_r = \dfrac{U_b H}{|\Gamma|}$, dimensionless background flow.

For the background-flow-dominated regime, we choose U_b as the characteristic velocity, and the parameters include:

3. $Re = \dfrac{U_b H}{\nu}$, the Reynolds number.
4. $\Gamma_r = \dfrac{\Gamma}{U_b H}$, dimensionless vortex strength.

Γ_r can be positive or negative depending on the inflow vortex street type. By definition, U_r and $|\Gamma_r|$ are less than or equal to 1. Multiple Reynolds numbers have also been used to describe flows induced by cylinders[51] and flapping bodies.[52]

In experiments, it would be difficult to control all the parameters (Γ, U_b, S_a, S_b) independently as we described in the vortex-blob model. A series of work has been conducted on the relationships between those parameters, and experimental data and empirical results have provided some typical values for them. Here, we discuss two ways of generating vortex streets and show how to compute the vortex street parameters of our model from experimental measurements.

The regular von Kármán street can be generated by flow past a circular cylinder. In this case, the far-field flow velocity U_∞ and the cylinder's diameter D are the two main control parameters in the experiments, and the vortex street can be altered by changing these two quantities. For instance, the vertical spacing between the vortices b can be approximated by the diameter D.[53,54] The ratio of the vertical to horizontal spacing $b/a = S_b/S_a$ is around 0.28 given by the von Kármán instability analysis[53] and around 0.26 by Kronauer's instability analysis.[54] The strength of the vortices is predicted in the work of Berger and Wille[55] as $\Gamma \approx 0.395 U_\infty D/St$ for flow past a circular cylinder at low Reynolds numbers (less than 200) where St is the Strouhal number. The value of St depends on the Reynolds number and ranges between 0.1 and 0.2 for a large range of Re.[56] Then, the vortex strength is approximately $2U_\infty D$ to $4U_\infty D$. The velocity of the vortex blob U is approximately $0.89U_\infty$ at $Re \approx 20\,000$ according to Bearman.[57] Therefore, given the values of a, b, Γ, and U_∞, the prescribed background flow can be obtained by $U_b = U - \dfrac{\Gamma}{2a} \tanh \dfrac{\pi b}{a}$.

A reverse von Kármán street can be generated by a heaving rigid foil. In this case, the vortices' shedding frequency f, the far-field flow velocity U_∞, and the heaving amplitude A are the main control parameters in the experiments. In one setup, it was shown that these three parameters must satisfy the relation $St_A = \dfrac{2fA}{U} > 0.18$ to ensure the generation of a reverse von Kármán street at the foil's trailing edge.[18,19] The vertical spacing can be approximated by the amplitude A and the background flow U_b is close to the far-field velocity U_∞. If we ignore the vortex shedding from the leading edge,[18] the circulation of the vortex at the trailing edge can be approximated by $\Gamma \approx \dfrac{1}{2}\pi^2 A^2 f^2$. Finally, the horizontal spacing can be obtained by solving the following nonlinear equation: $af = U_b + \dfrac{\Gamma}{2a} \tanh \dfrac{\pi b}{a}$ as a defines the period length of the vortex streets.

III. NUMERICAL METHODS

We design our numerical scheme to solve Navier-Stokes Equations (23) and (24) accurately and efficiently in the regime of laminar flow. We discretize the equations with an implicit Crank-Nicolson scheme to avoid the time step constraints of fully explicit schemes for the Navier-Stokes equations[58,59] and linearize the nonlinear advection term by a second-order extrapolation from previous time steps,

$$\mathbf{u}^{n+1/2} = \frac{3}{2}\mathbf{u}^{n} - \frac{1}{2}\mathbf{u}^{n-1}. \tag{26}$$

At the first step, we use a first-order extrapolation $\mathbf{u}^{1/2} = \mathbf{u}^0$ to obtain $\mathbf{u}^1$ and then correct the results by taking $\mathbf{u}^{1/2} = \frac{1}{2}(\mathbf{u}^0 + \mathbf{u}^1)$, which is also a second-order extrapolation. Spatial derivatives are discretized with a second-order difference scheme except at the channel walls where a fourth-order Briley's formula is used.

With the linearization of the advection term, ω and ψ are coupled only through Briley's formula. If we place the boundary conditions in a specific order in the system of equations, we can decouple the two terms with a computational cost of $O(NM)$ and solve them separately (we refer to Appendix A for more details). This linearization may be expected to cause an instability when dt is large or the flow changes rapidly. However, we find that for most parameters in the region of interest, a time step of $dt = 1/128$ is good enough for a stable result.

Since the incoming vortex street is time-periodic, we expect that the channel flow also converges to a time-periodic solution whose period is that of the incoming flow, given by $\tau_p = S_a/U$. In the simulation, we start from zero initial flow and evolve the flow with our time-marching scheme until it converges to a time-periodic state. The vorticity profiles at the end of each period $\omega^{k\tau_p}$, $k = 0, 1, \ldots$ are used for comparison, and the simulation is terminated when $\|\omega^{k\tau_p} - \omega^{(k-1)\tau_p}\|_2 \le 10^{-8}$. We find that for a grid size of 513×129 and $dt = 1/128$, it generally takes fewer than 30 periods for the channel flow to become time-periodic starting from zero flow. Convergence studies are performed for solutions at fixed times. We only obtain a convergence order between 1 and 2 for both time and space, because the problem is singular at the leading edge of the channel and in the initial condition. For smooth problems, second-order convergence is obtained for both time and spatial variables. Details about the numerical methods and convergence studies are provided in Appendices A and B.

IV. RESULTS AND DISCUSSION

Now we present the channel flows that result from the two types of incoming flows: reverse and regular von Kármán streets. Unlike flows in an unbounded region, the flow behaves dramatically different for these two types of incoming flows due to the existence of the walls. We are mainly interested in the periodic-state solutions. Therefore, all the results presented in this section are obtained by the above numerical method and are in the time-periodic state unless stated.

A. Reverse von Kármán street

In the reverse von Kármán street case, two staggered rows of vortex blobs enter the channel periodically with positive circulations in the upper row and negative circulations in the lower row.

We show the contour plots of the vorticity and the speed $\|\mathbf{u}\| = \sqrt{u^2 + v^2}$ of the flow over the whole channel at one time instant (beginning of a period) in Figure 3. The plots are obtained with $U_r = \Gamma_r = 1$, which implies $U_b = \Gamma = 1$.

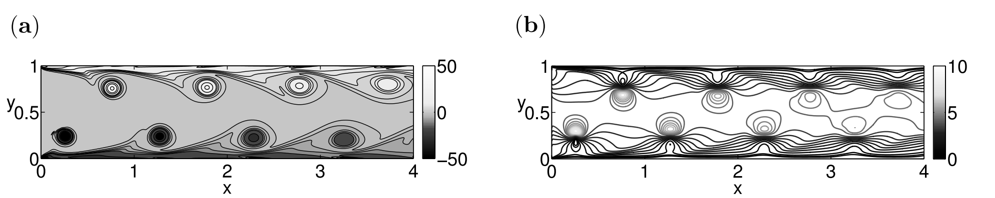

FIG. 3. Contour plots of vorticity (a) and flow speed (b) obtained with $Re = 1000$, $S_a = 1$, $S_b = 0.5$, $U_r = 1$, and $\Gamma_r = 1$. (a) Region shades give vorticity values; (b) line shades give flow speed values.

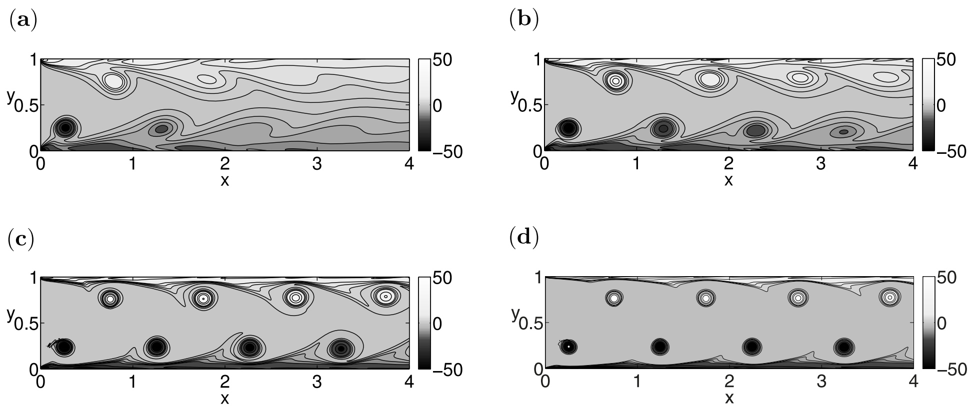

FIG. 4. Instantaneous contour plots of vorticity obtained with $S_a = 1$, $S_b = 0.5$, $U_r = 1$, $\Gamma_r = 1$, and (a) Re = 200, (b) Re = 500, (c) Re = 2000, and (d) Re = 5000.

In Figure 3(a), we notice that the vortex blobs mainly move in the downstream direction and the structure of the reverse von Kármán vortex street is maintained in the channel. The blobs diffuse in the channel, and their shape approximates a semicircle due to the walls' presence. Each blob induces an upstream flow between the blob itself and the wall and decreases the speed of the flow in that region, as shown in Figure 3(b). This flow thus generates opposite-signed vorticity in the boundary layer adjacent to the corresponding vortex blob, which leads to alternating positive and negative vorticities in the boundary layer.

These properties hold not only for this particular parameter set. We observe the same phenomena for a wide range of Re, S_a, S_b, U_r, and Γ_r in the reverse von Kármán street cases. In Figures 4–7, we show the time instantaneous vorticity contours of the flows at various dimensionless parameter values, and we take all the contour curves at the same values for comparison.

In Figure 4, we vary the Reynolds number from 200 to 5000 and keep the other parameters unchanged. The diffusion effect becomes weaker as the Reynolds number increases. Therefore, we observe stronger vortex blobs as well as stronger and thinner boundary layers in the channel as Re becomes larger.

In Figure 5, we change the value of S_b, while keeping the other parameters fixed. S_b defines the vertical space between two incoming blobs, and therefore cannot exceed 1. In the computation, the vortex blob has $\delta = 0.05$ and we take S_b no larger than 0.8 and only consider situations when the blobs do not contact the wall.

When S_b is zero, all the negative and positive blobs are aligned on the centerline of the channel and the blob induced velocity is zero at each blob center at the inflow. They rely on the background

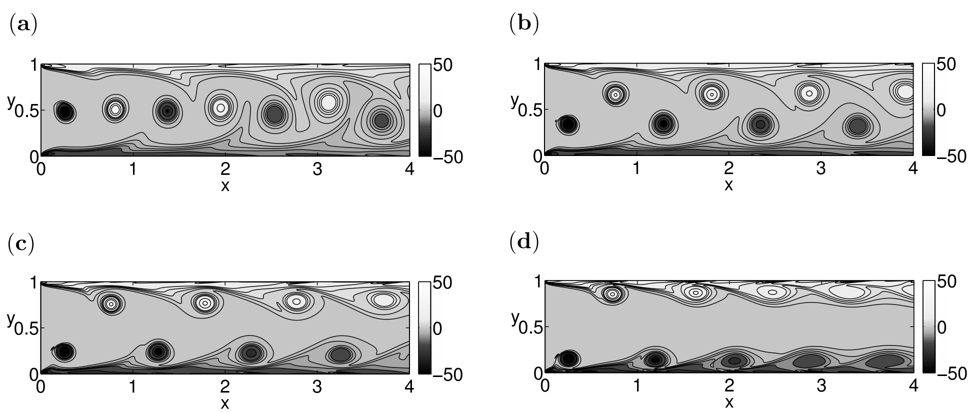

FIG. 5. Instantaneous contour plots of vorticity obtained with $Re = 1000$, $S_a = 1$, $U_r = 1$, $\Gamma_r = 1$, and (a) $S_b = 0$, (b) $S_b = 0.3$, (c) $S_b = 0.5$, and (d) $S_b = 0.7$.

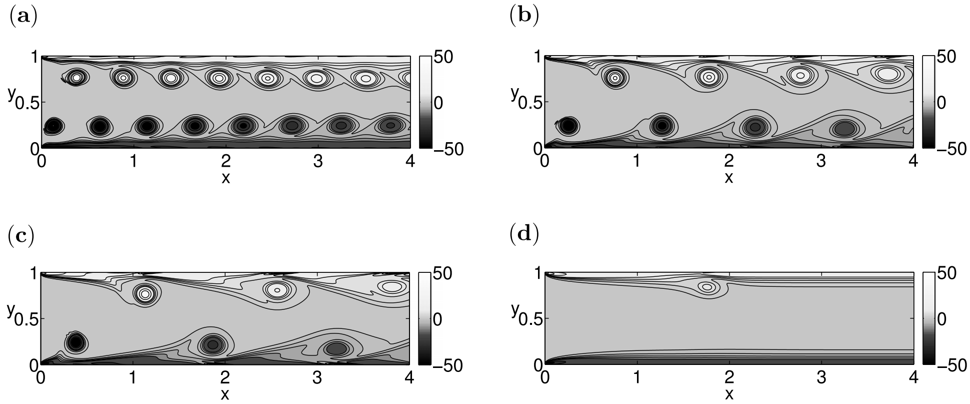

FIG. 6. Instantaneous contour plots of vorticity obtained with $Re = 1000$, $S_b = 0.5$, $U_r = 1$, $\Gamma_r = 1$, and (a) $S_a = 0.5$, (b) $S_a = 1$, (c) $S_a = 1.5$, and (d) $S_a = \infty$.

flow to be advected into the channel. However, when the blobs enter the channel, there will only be a finite number of blobs in the channel and their induced velocities do not cancel with each other. The blobs will shift away from the centerline and form a street similar to the reverse von Kármán street as shown in Figure 5(a). There is no difference between the reverse and regular von Kármán street inflows when $S_b = 0$, as we can view the reverse von Kármán street case as the regular one shifted by a half period in time. As S_b increases, the vortex blobs are closer to the wall boundary and stronger interactions with the boundary layer occur.

In Figure 6, we vary the value of S_a and fix the other parameters. S_a defines the horizontal spacing between two blobs and determines the length of the period. When S_a tends to infinity, only a single vortex blob is in the channel as shown in Figure 6(d) and the time-periodicity is violated. We notice that the blob is closer to the wall compared to the one at the same x position in panel (b) although they are at the same height at the entrance of the channel. This indicates that the interaction between blobs helps to maintain the vertical positions of the blobs. As S_a increases, the period length also increases, which leads to fewer blobs in the channel.

In Figure 7, we change the value of Γ_r and U_r and fix the other parameters. In the background-flow-dominated regime, the vortex blobs become weaker as Γ_r decreases. In panel (a), the boundary layer behaves similarly to the Prandtl boundary layer solution with small perturbations to the main flow. In the vortex-dominated regime, we fix the strength of the vortex blob and decrease the background flow U_r from 1 to 0. The background flow generates negative vorticity in the lower boundary layer and positive vorticity in the upper layer. Thus, we observe a weaker Prandtl boundary layer in

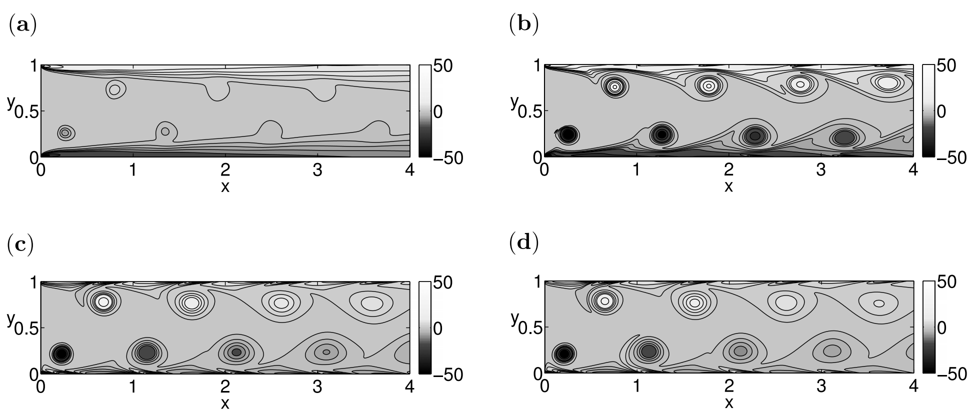

FIG. 7. Instantaneous contour plots of vorticity obtained with $Re = 1000$, $S_a = 1$, $S_b = 0.5$ and (a) $\Gamma_r = 0.1$, $U_b = 1$; (b) $U_r = U_b = 1, \Gamma_r = \Gamma = 1$; (c) $U_r = 0.1$, $\Gamma = 1$; (d) $U_r = 0$, $\Gamma = 1$.

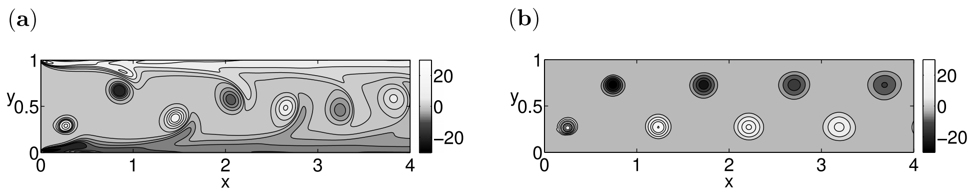

FIG. 8. (a) Instantaneous contour plots of vorticity obtained with $Re = 1000$, $S_a = 1$, $S_b = 0.5$, $\Gamma_r = -0.5$, and $U_b = 1$. (b) Instantaneous contour plots of vorticity obtained with the stress-free boundary condition and the same parameters as (a).

panel (c) compared to panel (b) as U_r decreases. Meanwhile, the blobs also generate oppositely signed vorticity which is weakened by the background flow. Therefore, we find stronger opposite-signed vorticity with smaller U_r. For reverse von Kármán street inflow, the blob-induced velocity at the blob's center is in the downstream direction, which allows the blobs to enter the channel with $U_r = 0$, shown in panel (d). We observe two oppositely signed regions of vorticity separated from the wall behind the first positive blob and the second negative blob. The separated vorticity is much weaker than the vortex blobs and is smoothed out quickly in the channel.

B. Regular von Kármán street

In the regular von Kármán street case, two staggered rows of vortex blobs enter the channel periodically with negative circulations in the upper row and positive circulations in the lower row. In contrast to the reverse von Kármán street case where the spatial structure is maintained in the channel, the vortex street is not stable for regular von Kármán street inflow.

We show the instantaneous contour plots of the vorticity for a certain set of parameters in Figure 8(a) and observe that the entering vortices move away from the wall, and the structure of the incoming flow is altered. We see a "crisscross" motion of the rows of vortices which is in agreement with earlier works.[32–34,60] The crisscross motion happens mainly due to the interaction between the incoming vortex blobs and the wall-separated vorticity. Each vortex blob induces a flow in the downstream direction and increases the flow speed in the region between the blob and the wall. Therefore, the vortex blob reinforces the boundary layer and leads to strong vorticity with opposite sign on the wall which then separates. The interaction between the incoming vortex blob and the separated vorticity of the adjacent wall boundary layer then pushes the negative vortex blob downwards and the positive blob upwards. The blobs thus cross the centerline and exchange their positions in the channel. Afterwards, the positive blobs remain in the upper half and the negative blobs in the lower half, forming a street with a structure similar to that of the reverse von Kármán street.

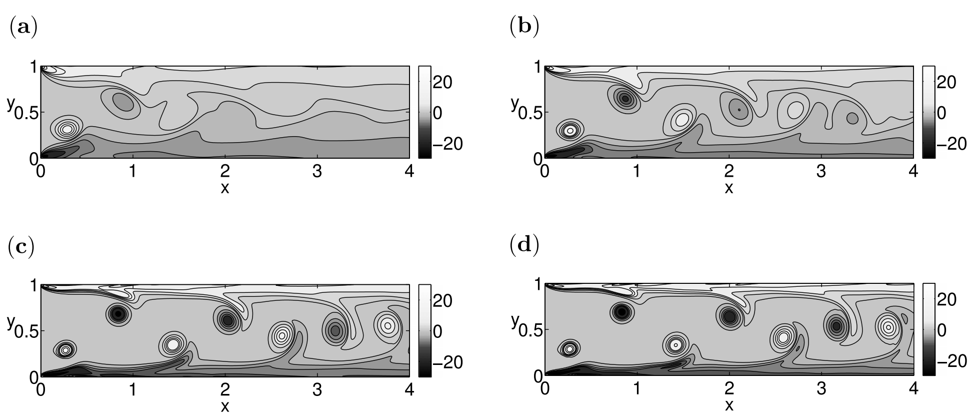

FIG. 9. Instantaneous contour plots of vorticity obtained with $\Gamma_r = -0.5$, $S_a = 1$, $S_b = 0.5$, $U_b = 1$, and (a) Re = 200, (b) Re = 500, (c) Re = 1500, and (d) Re = 2000.

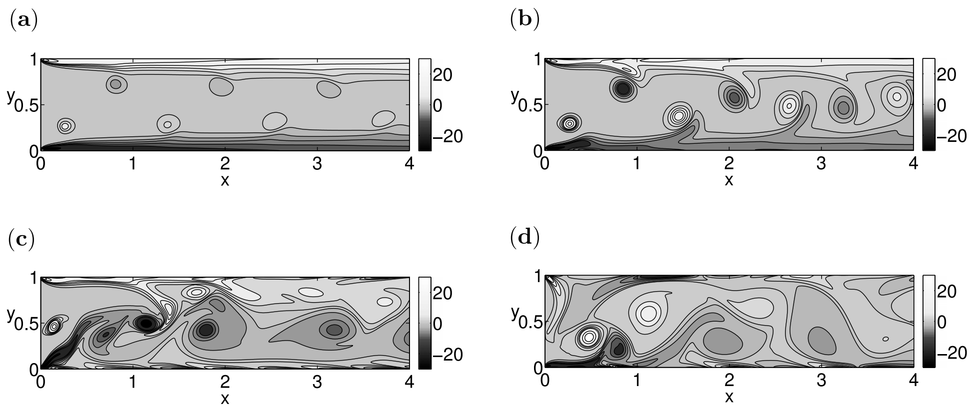

FIG. 10. Instantaneous contour plots of vorticity obtained with $Re = 1000$, $S_a = 1$, $S_b = 0.5$, and (a) $\Gamma_r = -0.1$, $U_b = 1$; (b) $\Gamma_r = -0.5$, $U_b = 1$; (c) $\Gamma_r = \Gamma = -1$, $U_b = U_r = 1$; (d) $U_r = 0.6$, $\Gamma = -1$.

To test this hypothesis, we impose a stress-free condition for u on the wall as $\dfrac{\partial u}{\partial y} = 0$ instead of the no-slip condition. This condition plus the no-penetration condition leads to $\omega = \nabla \times \mathbf{u} = -u_y + v_x = 0$ at the wall boundary which prohibits the generation and separation of wall vorticity. A similar strategy was applied by Camarri and Giannetti[33] to examine the vorticity field in flow past a confined cylinder. In Figure 8(b), we show the instantaneous vorticity contours obtained with same parameters as in panel (a) but with the stress-free boundary condition. By eliminating the wall vorticity, it is clear that the inversion of vortices does not happen.

We also consider the effect of the parameters Re, S_b, S_a, U_r, and Γ_r on the flow structures. In Figures 9–13, we show the instantaneous vorticity contours for various parameter sets, and we take all the contours at the same values for comparison. We find that in the regular von Kármán street cases, physical parameters play a significant role in determining the flow structures and dynamics, which is in contrast to the reverse von Kármán street cases.

In Figure 9, we vary the Reynolds number from 200 to 2000 and keep the other parameters unchanged. As the Reynolds number increases, diffusion becomes weaker and the strengths of the vortex blobs are maintained for longer distances in the channel, which leads to stronger vorticity separated from the walls.

In Figure 10, we vary Γ_r and U_r with the other parameters fixed. We first consider the background-flow-dominated regime where $U_b = 1$ and vary Γ_r from -1 to 0. We observe clearly distinct results for different Γ_r in Figures 10(a)–10(c). When Γ_r is small as shown in Figure 10(a), the blobs move towards the centerline but do not cross it in the channel. As the magnitude of Γ_r increases, the flow becomes more and more irregular. We define the time-averaged vorticity over one time-period τ_p as

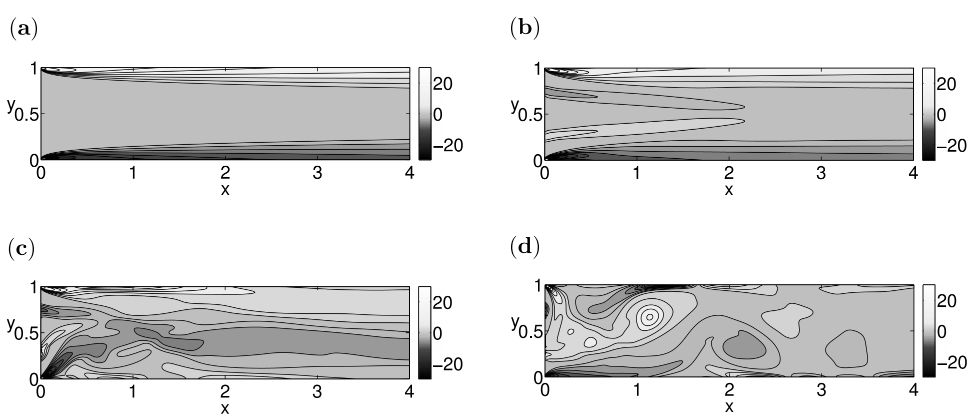

FIG. 11. Contour plots of time-averaged vorticity obtained with $Re = 1000$, $S_a = 1$, $S_b = 0.5$, and (a) $\Gamma_r = -0.1$, $U_b = 1$; (b) $\Gamma_r = -0.5$, $U_b = 1$; (c) $\Gamma_r = \Gamma = -1$, $U_b = U_r = 1$; (d) $U_r = 0.6$, $\Gamma = -1$.

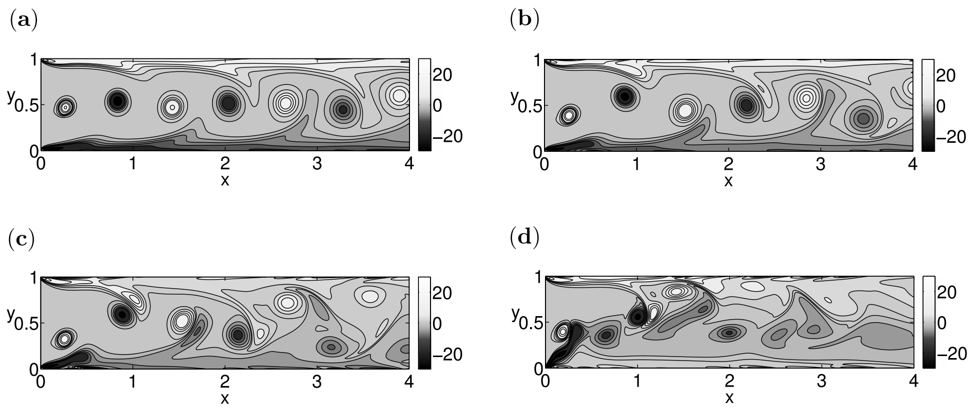

FIG. 12. Instantaneous contour plots of vorticity obtained with $Re = 1000$, $\Gamma_r = -0.75$, $U_b = 1$, $S_a = 1$, and (a) $S_b = 0.1$, (b) $S_b = 0.3$, (c) $S_b = 0.5$, and (d) $S_b = 0.7$.

$\overline{\omega} = \dfrac{1}{\tau_p} \displaystyle\int_0^{\tau_p} \omega(\cdot, t) dt$ and show the corresponding contour plots in Figure 11. We note that the time period $\tau_p = S_a/U$ is defined according to the inflow condition.

We define the flow to be a "symmetric street" if $\overline{\omega}$ is anti-symmetric with respect to the centerline ($y = 0.5$). This holds for flows with $\Gamma_r = -0.1$ and -0.5. Intuitively, symmetry is possible because the time-averaged inflow and the geometric shape of the channel are symmetric. However, we find that when the interactions of the vortex blobs and the boundary layers are sufficiently strong, the average flow becomes asymmetric as shown in Figures 11(c) and 11(d), and we define such cases as "asymmetric streets." In this case, the vorticity separated from the wall is comparable in strength to the vortex blobs, and the interaction destroys the structure of the vortex streets.

In the regular von Kármán street inflow, the induced velocity at the center of the blobs is in the upstream direction, and therefore, a positive background flow is necessary for the blobs to enter the channel. In fact, in the vortex-dominated regime, U_r must satisfy the following bounds depending on the geometric parameters S_a and S_b to guarantee a downstream velocity of the vortex blobs:

$$1 \geq U_r \geq \frac{\tanh\left(\pi S_b / S_a\right)}{2 S_a}. \tag{27}$$

For parameter values $S_a = 1$ and $S_b = 0.5$, we find that the flow is always asymmetric in the vortex-dominated regime for $Re \geq 250$.

In Figure 12, we vary the value of S_b and keep the other parameters fixed. As S_b increases, the vortex blobs are closer to the wall and their interactions with the wall vorticity are stronger as well.

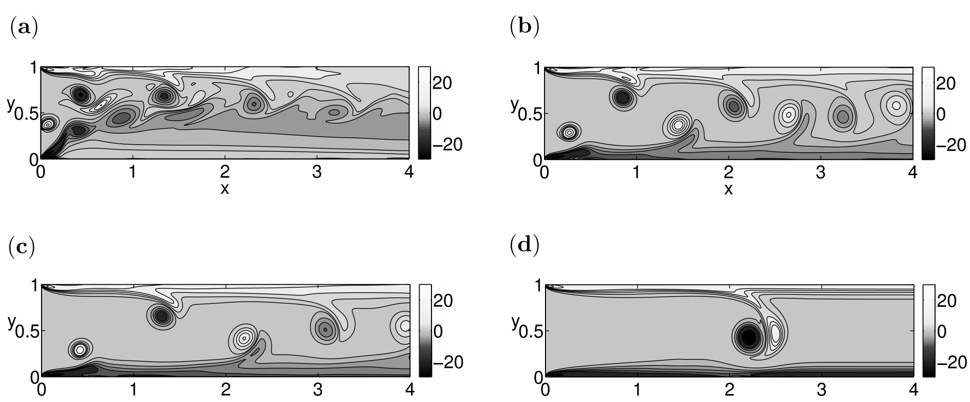

FIG. 13. Contour of vorticity obtained with $Re = 1000$, $\Gamma_r = -0.5$, $U_b = 1$, $S_b = 0.5$, and (a) $S_a = 0.5$, (b) $S_a = 1.0$, (c) $S_a = 1.5$, and (d) $S_a = \infty$.

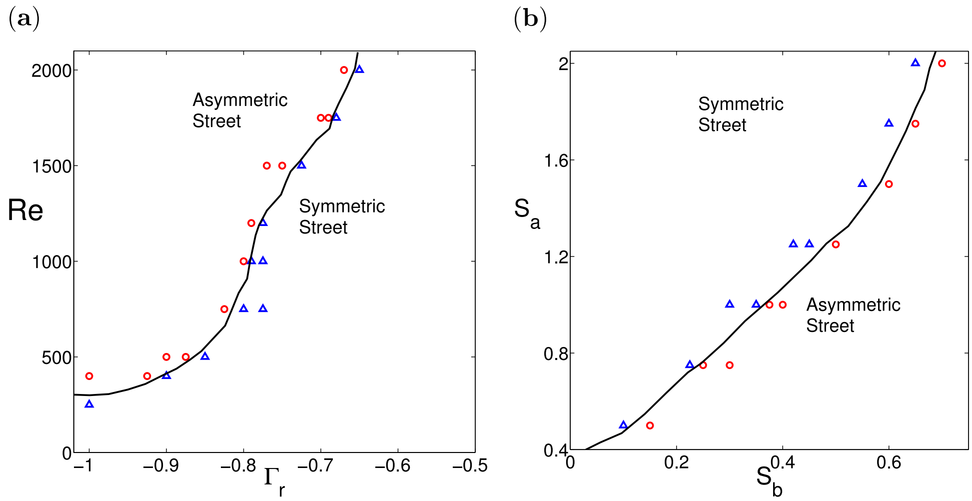

FIG. 14. Diagram of vortex street type for (a) Re and Γ_r with $S_a = 1$ and $S_b = 0.5$. (b) S_b and S_a with $Re = 1000$ and $\Gamma_r = -1$, $U_b = 1$. The triangles indicate numerical results giving symmetric streets and the circles indicate asymmetric streets. The solid line indicates the transition boundary.

Therefore, we expect to observe more irregular streets when S_b becomes larger. Figures 12(a)–12(c) show contour plots of vorticity in symmetric streets and Figure 12(d) shows an asymmetric street.

In Figure 13, we change the value of S_a and keep the other parameters unchanged. The vortex blobs are closer to each other as S_a decreases, which leads to more irregular streets since the interactions are stronger, as shown in Figure 13(a). When S_a tends to infinity, only a single vortex blob is present in the channel. The blob crosses the centerline under the pure influence of the wall vorticity without other blobs.

In Figure 14, we plot a diagram of different types of vortex streets corresponding to the fluid parameters Re, Γ_r, S_a, and S_b. In general, the flow transitions from symmetric to asymmetric as Re increases, Γ_r becomes more negative, S_a decreases, and S_b increases. We only consider the background-flow-dominated regime in panel (a) and note that for a given Re, if the flow is asymmetric for $\Gamma_r = -1$, then all flows in the vortex-dominated regime are also asymmetric.

For symmetric streets, the time-averaged vorticity $\overline{\omega}$ is always zero along the centerline of the channel. Right above the centerline, $\overline{\omega}$ is negative at the entrance of the channel and gradually becomes positive. Similarly, $\overline{\omega}$ is positive right below $y = 0.5$ and decreases along the channel to negative values. We define the exchange distance X_e as the horizontal position where $\overline{\omega}$ inverts its positive and negative layers in the channel,

$$X_e = \inf\{x : \overline{\omega}(x, 0.5 + h) \geq \epsilon\}. \tag{28}$$

Here, ϵ is a small threshold and is chosen to be 10^{-6} in the simulation. h is the y-direction grid spacing and $0.5 + h$ is one grid point above the centerline. By the symmetry of $\overline{\omega}$, this definition is the same as $X_e = \inf\{x : \overline{\omega}(x, 0.5 - h) \leq -\epsilon\}$. In Figure 15, we use the contour plots of $\overline{\omega}$ at $Re = 1000$, $S_a = 1$, $S_b = 0.5$, $\Gamma_r = -0.5$, and $U_b = 1$ to illustrate the position of X_e. This definition of X_e is similar to the x_{inv} quantity defined by Camarri and Giannetti[33] as the cross section in x at which positive and

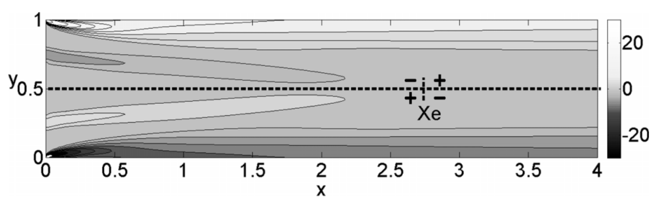

FIG. 15. Contour plots of $\overline{\omega}$ at $Re = 1000$, $S_a = 1$, $S_b = 0.5$, $\Gamma_r = -0.5$, and $U_b = 1$. The centerline $y = 0.5$ is shown with a horizontal dashed line. Above the centerline, negative vorticity enters the channel and increases to positive values after X_e. Below the centerline, positive vorticity enters the channel and decreases to negative values after X_e.

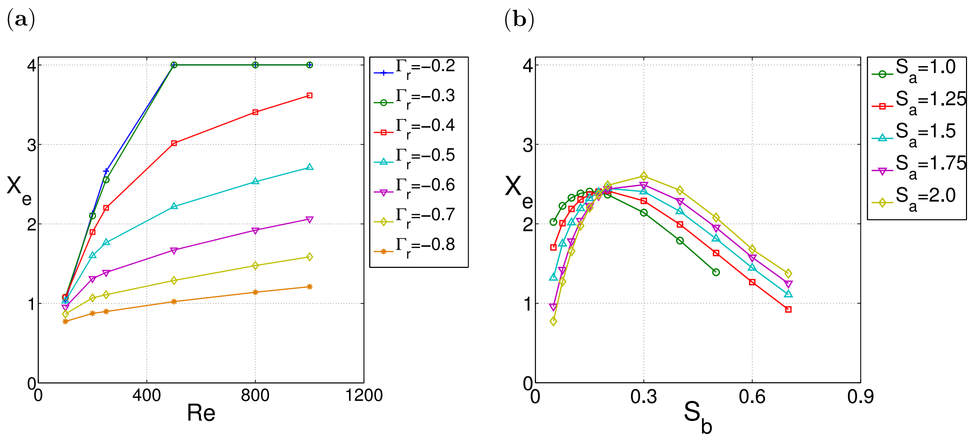

FIG. 16. (a) X_e vs. Re with $\Gamma_r = -0.2, -0.3, -0.4, -0.5, -0.6, -0.7, -0.8$, $U_b = 1$, $S_a = 1$, and $S_b = 0.5$; (b) X_e vs. S_b with $S_a = 1, 1.25, 1.5, 1.75, 2$, $\Gamma_r = -0.75$, $U_b = 1$, and $Re = 1000$.

negative vortex trajectories intersect. X_e depends on Re, Γ_r, S_b, and S_a, and we plot X_e versus different parameters in Figure 16. We only consider X_e for symmetric streets. The missing data points in the graph indicate that the street is asymmetric for that particular parameter set. We define $X_e = 4$ if the positive and negative blobs do not cross the centerline in the channel.

In panel (a), we find that X_e increases when the Reynolds number increases. This is in contrast to the observation by Camarri *et al.*[33] where they found the inverted position monotonically decreases with Re. However, their work focuses on a narrower range of Reynolds numbers (50-170) with a square cylinder as the vortex generator, which is different from our model. When Γ_r becomes more negative, the vortex blobs and the interactions with the separated vorticity are stronger, resulting in a smaller exchange distance.

When S_b increases, the blobs are closer to the wall which makes them move towards the centerline faster, as the wall interactions are stronger. On the other hand, the blobs must also travel further to invert their positions as they are further moved from the centerline. Therefore, in panel (b), the maximum X_e is obtained at a moderate value of S_b instead of at the boundaries, and we find that X_e decays linearly with S_b beyond the maximum.

The effect of S_a on X_e is also complicated. When $S_b < 0.175$, we notice that X_e decreases with S_a, and when $S_b \geq 0.2$, it increases with S_a. When S_b is sufficiently small and the blob is close to the centerline, the inversion location mainly depends on the speed of the vortex blob. For negative Γ_r, this speed increases with S_a which leads to smaller X_e. When S_b is large, the blobs are pushed towards the centerline through their interactions with the boundary vorticity. The exchange distance X_e is more influenced by the strength of these interactions. We therefore observe smaller X_e with smaller S_a as the interactions between the blobs and the separated vorticity are stronger.

V. CONCLUSION

In this work, we have numerically studied the effect of wall confinement on vortex street dynamics in a channel flow. Instead of modelling a specific vortex generator, we model typical wakes as smoothed von Kármán vortex streets with various vortex strengths and geometries and apply them as inflow boundary conditions. This approximation allows us to explore a large parameter space of $\{Re, \Gamma_r, U_r, S_b, S_a\}$ and classify the vortex dynamics of the channel flows.

When the inflow is a reverse von Kármán street, we find that vortex blobs maintain their spatial structure from the inflow and mainly move in the downstream direction. When the inflow is a regular von Kármán street, we find that the vortex blobs move towards the centerline and exchange their positions in the channel. This "criss-cross" motion is due to the interactions between the blobs and the separated vorticity from the wall. The location where the inversion happens depends on the strength of this interaction, as well as the momentum of the vortex blobs and the geometry of the incoming streets.

For the regular von Kármán streets, different parameters lead to very different flow profiles. We have classified them as symmetric or asymmetric streets depending on the symmetry of the time-averaged vorticity. The transition to asymmetry happens when the interactions between the blobs and the separated vorticity are sufficiently strong to destroy the spatial structure of the inflow. We have determined the transition location in certain cross sections of $\{Re, \Gamma_r, S_b, S_a\}$ space. In general, the flow transitions to asymmetric as Re increases, Γ_r becomes more negative, S_a decreases, and S_b increases.

An extension of this work is to consider the vortex dynamics in a three-dimensional channel. This requires an understanding of the vortex wakes behind different vortex generators in 3-D flow. Another interesting topic is to apply the current fluid model to study the vorticity-enhanced heat transfer process. For example, Hildago *et al.*[61] used a piezoelectric driven reed to generate a reverse von Kármán street in a heated channel and found a large increase in the coefficient of performance (the ratio of the thermal power dissipation to the mechanical power used to drive the flow). Shoele and Mittal[62] studied heat transfer of a self-oscillating flexible reed in a channel flow which generated a regular von Kármán vortex wake. They reported that the optimal thermal performance is achieved when the vortex wake disrupts the boundary layer but does not have strong vortices. A better understanding of the vortex dynamics in a channel flow may suggest vortex generators with improved thermal performance.

ACKNOWLEDGMENTS

We acknowledge support from NSF-DMS, Grant No. 1329726 and a Sloan Research Fellowship (S.A.).

APPENDIX A: NUMERICAL METHODS

In this section, we show the details of our numerical methods. Equations (23) and (24) are discretized with an linearized implicit Crank-Nicolson scheme. Denoting the current time step as n, the time discretization is

$$\frac{\omega^{n+1} - \omega^n}{dt} + \frac{1}{2}\mathbf{u}^{n+1/2} \cdot (\nabla\omega^{n+1} + \nabla\omega^n) = \frac{1}{2}\frac{1}{Re}(\Delta\omega^{n+1} + \Delta\omega^n), \tag{A1}$$

$$-\Delta\psi^{n+1} = \omega^{n+1}. \tag{A2}$$

With the linearization of the advection term, we see that Equations (A1) and (A2) are coupled only through Briley's formula and if we place the boundary conditions in a specific order in the system of equations, we can write the linear system as follows:

$$\left(\begin{array}{c|c}
B & I \\ \hline
0 & I(\omega_{in}) \\
-\Delta & I \\
adv. & cI \\ \hline
B & I \\ \hline\hline
I(\psi_w) & 0 \\ \hline
I(\psi_{in}) & 0 \\
0 & L \\
0 & adv. \\ \hline
I(\psi_w) & 0
\end{array}\right)
\left(\begin{array}{c}
\\ \\ \psi \\ \\ \\ \hline\hline \\ \\ \omega \\ \\ \\
\end{array}\right)
=
\left(\begin{array}{c}
0 \\ \hline
\omega_{in} \\
0 \\
0 \\ \hline
0 \\ \hline\hline
\psi_w \\ \hline
\psi_{in} \\
0 \\
0 \\ \hline
\psi_w
\end{array}\right)$$

Here, B stands for Briley's formula, $L = -\Delta + \mathbf{u}\cdot\nabla$, $c = -dt\,\bar{u}$, adv. denotes the advective derivative condition, $I(\omega_{in})$ and $I(\psi_{in})$ are the identity matrices from the inflow conditions on ω and ψ, and $I(\psi_w)$ is the identity matrix from the wall boundary condition on ψ. The linear system can be written in block matrix form as

$$\begin{pmatrix} A_{11} & A_{12} \\ A_{21} & A_{22} \end{pmatrix}\begin{pmatrix} \psi \\ \omega \end{pmatrix} = \begin{pmatrix} b_1 \\ b_2 \end{pmatrix}. \tag{A3}$$

The problem can be solved by a block LU decomposition which leads to the linear system,

$$(A_{21} - A_{22}A_{12}^{-1}A_{11})\psi = b_2 - A_{22}A_{12}^{-1}b_1. \tag{A4}$$

The matrix in Equation (A4) can be formed explicitly as all four blocks are sparse matrices and the right-upper block A_{12} is a diagonal matrix given $\bar{u} \neq 0$. A_{21} has only $2N + M + 1$ nonzeros on the diagonal, and both A_{11} and A_{22} are close to pentadiagonal matrices except at boundary points. The computational cost to explicitly form the matrix in Equation (A4) is $O(NM)$. The linear matrix can be solved by an iterative method such GMRES with a preconditioner.[63,64] However, we find a direct solver is sufficiently fast and scalable. For a spatial grid of 513×129 and $dt = 1/128$, it takes about 150 s to run the simulation for one period on a single processor. The computational cost scales approximately as $(NM)^{1.3}$.

Once ψ is obtained, we obtain ω by the following equation:

$$\omega = A_{12}^{-1}b_1 - A_{12}^{-1}A_{11}\psi. \tag{A5}$$

Since A_{12} is a diagonal matrix, only matrix-vector multiplication is required to obtain ω from ψ.

APPENDIX B: CONVERGENCE STUDY

In this section, we display the results of convergence studies for time and space. For a smooth problem, second order convergence is expected for both time and spatial variables. For all the numerical results obtained here, we use the following parameters: the length of the channel $L = 4$, the height of the channel $H = 1$, $S_a = 1$, and $S_b = 0.5$. We choose $U_b = \Gamma = 1$ for the reverse von Kármán streets and $U_b = 1, \Gamma = -0.5$ for regular von Kármán street, and $Re = 500$ for both cases.

In Tables I and II, we show the convergence results for spatial variables by comparing the value of ω obtained at certain locations and a fixed time instant $t = 6\tau_p$, where τ_p is the time period. These locations include interior points at the center line of the channel $(x, y) = (2, 0.5)$ and near one of the vortex blobs $(x, y) = (2, 0.25)$ and the boundary point at $(x, y) = (4, 0.5)$. Tables I and II show the results for reverse and regular von Kármán streets, respectively. The error and ratio are calculated by the following formula:

$$\text{error} = \left|\omega(dx) - \omega(\frac{dx}{2})\right|,$$

$$\text{ratio} = \frac{|\omega(dx) - \omega(\frac{dx}{2})|}{|\omega(\frac{dx}{2}) - \omega(\frac{dx}{4})|},$$

and it should be 4 when second order convergence is achieved.

TABLE I. dx-convergence in ω for reverse von Kármán street.

	(x, y) = (2, 0.5)			(x, y) = (2, 0.25)			(x, y) = (4, 0.5)		
dx	$\omega(x,y)$	Error	Ratio	$\omega(x,y)$	Error	Ratio	$\omega(x,y)$	Error	Ratio
2^{-6}	6.022×10^{-3}	2.196×10^{-3}	2.8	−2.966	3.124×10^{-3}	2.5	5.326×10^{-2}	8.167×10^{-3}	4.5
2^{-7}	8.218×10^{-3}	7.759×10^{-4}	3.5	−2.969	1.237×10^{-3}	2.3	4.509×10^{-2}	1.830×10^{-3}	1.4
2^{-8}	8.994×10^{-3}	2.248×10^{-4}	…	−2.970	5.289×10^{-4}	…	4.326×10^{-2}	1.292×10^{-3}	…
2^{-9}	9.219×10^{-3}	…	…	−2.970	…	…	4.197×10^{-2}	…	…

TABLE II. dx-convergence in ω for regular von Kármán street.

	(x, y) = (2, 0.5)			(x, y) = (2, 0.25)			(x, y) = (4, 0.5)		
dx	$\omega(x, y)$	Error	Ratio	$\omega(x, y)$	Error	Ratio	$\omega(x, y)$	Error	Ratio
2^{-6}	−3.269	0.940	1.8	−0.355	0.119	2.6	1.493	0.511	1.3
2^{-7}	−4.209	0.537	2.4	−0.236	4.523×10^{-2}	2.8	0.982	0.395	6.5
2^{-8}	−4.746	0.225	...	−0.191	1.627×10^{-2}	...	0.586	6.069×10^{-2}	...
2^{-9}	−4.971	...	...	−0.175	...	...	0.526	...	...

TABLE III. dt-convergence in ω for reverse von Kármán street.

	(x, y) = (2, 0.5)			(x, y) = (2, 0.25)			(x, y) = (4, 0.5)		
dt	$\omega(x, y)$	Error	Ratio	$\omega(x, y)$	Error	Ratio	$\omega(x, y)$	Error	Ratio
2^{-6}	5.762×10^{-3}	2.458×10^{-3}	3.6	−3.027	5.341×10^{-2}	7.0	2.952×10^{-2}	1.556×10^{-2}	2.4
2^{-7}	8.218×10^{-3}	6.805×10^{-4}	5.4	−2.974	7.706×10^{-3}	3.1	4.509×10^{-2}	6.567×10^{-3}	2.2
2^{-8}	8.994×10^{-3}	1.264×10^{-4}	...	−2.966	2.451×10^{-4}	...	5.166×10^{-2}	2.977×10^{-3}	...
2^{-9}	9.025×10^{-3}	...	...	−2.963	...	...	5.464×10^{-2}	...	...

As shown in Tables I and II, a convergence order between 1 and 2 is achieved. This is mainly caused by the leading edge singularity due to the violation of no-slip and no-penetration conditions of the inflow condition. If we consider a smooth problem where the inflow condition is given by a Poiseuille flow $u(y) = 6y(1-y), v = 0$, then a second order convergence can be achieved with the same numerical methods.

In Tables III and IV, we show the convergence results for time variables again by comparing the value of ω obtained at certain locations and the fixed time instant $t = 6\tau_p$. Tables III and IV show the results for the reverse and regular von Kármán streets, respectively. The error and ratio are calculated by the following formula:

$$\text{error} = \left|\omega(dt) - \omega\left(\frac{dt}{2}\right)\right|,$$
$$\text{ratio} = \frac{\left|\omega(dt) - \omega(\frac{dt}{2})\right|}{\left|\omega(\frac{dt}{2}) - \omega(\frac{dt}{4})\right|}.$$

As shown in Tables III and IV, the convergence ratios for some points are actually larger than 2. This may be caused by the sudden start of the fluids as the inflow changes abruptly from 0 to some nonzero values at $t = 0$. We also consider a smooth problem where the inflow condition is given by a combination of two Poiseuille flows $u(y,t) = 8e^{-t^3}y(1-y) + 6(1-e^{-t^3})y(1-y)$ and initially the flow in the channel is set to be $u(x,y,t) = 8y(1-y)$. The flow and its first three derivatives are continuous at $t = 0$. We observe a second order convergence in time for this smooth problem.

TABLE IV. dt-convergence in ω for regular von Kármán street.

	(x, y) = (2, 0.5)			(x, y) = (2, 0.25)			(x, y) = (4, 0.5)		
dt	$\omega(x, y)$	Error	Ratio	$\omega(x, y)$	Error	Ratio	$\omega(x, y)$	Error	Ratio
2^{-6}	−4.453	0.244	4.9	−0.243	6.987×10^{-3}	3.5	1.493	0.321	4.4
2^{-7}	−4.209	4.934×10^{-2}	6.9	−0.236	1.976×10^{-3}	5.5	0.982	7.407×10^{-2}	3.3
2^{-8}	−4.160	7.117×10^{-3}	...	−0.234	6.366×10^{-4}	...	1.056	2.449×10^{-2}	...
2^{-9}	−4.153	...	...	−0.233	...	...	1.080	...	...

[1] A. M. Jacobi and R. K. Shah, "Heat transfer surface enhancement through the use of longitudinal vortices: A review of recent progress," Exp. Therm. Fluid Sci. **11**(3), 295–309 (1995).
[2] J. G. Li, "A mechanism for heat transfer enhancements by vortex shedding," in *Fluids Engineering Division Conference, FED, San Diego, California* (ASME, 1996), Vol. 239, p. 533.
[3] M. Fiebig, P. Kallweit, N. Mitra, and S. Tiggelbeck, "Heat transfer enhancement and drag by longitudinal vortex generators in channel flow," Exp. Therm. Fluid Sci. **4**(1), 103–114 (1991).
[4] T. Açıkalın, S. V. Garimella, A. Raman, and J. Petroski, "Characterization and optimization of the thermal performance of miniature piezoelectric fans," Int. J. Heat Fluid Flow **28**(4), 806–820 (2007).
[5] D. Gerty, "Fluidic-driven cooling of electronic hardware," Ph.D. dissertation, Georgia Institute of Technology, 2008.
[6] A. Sharma and V. Eswaran, "Heat and fluid flow across a square cylinder in the two-dimensional laminar flow regime," Numer. Heat Transfer, Part A **45**(3), 247–269 (2004).
[7] P. G. Saffman, *Vortex Dynamics* (Cambridge Univ. Press, 1992).
[8] T. Sarpkaya and R. L. Schoaff, "Inviscid model of two-dimensional vortex shedding by a circular cylinder," AIAA J. **17**(11), 1193–1200 (1979).
[9] R. R. Clements, "An inviscid model of two-dimensional vortex shedding," J. Fluid Mech. **57**(2), 321–336 (1973).
[10] M. Kiya and M. Arie, "A contribution to an inviscid vortex-shedding model for an inclined flat plate in uniform flow," J. Fluid Mech. **82**(2), 223–240 (1977).
[11] J. H. Gerrard, "The mechanics of the formation region of vortices behind bluff bodies," J. Fluid Mech. **25**(02), 401–413 (1966).
[12] S. Tang and N. Aubry, "On the symmetry breaking instability leading to vortex shedding," Phys. Fluids **9**(9), 2550–2561 (1997).
[13] A. E. Perry, M. S. Chong, and T. T. Lim, "The vortex-shedding process behind two-dimensional bluff bodies," J. Fluid Mech. **116**, 77–90 (1982).
[14] H. Oertel, Jr., "Wakes behind blunt bodies," Annu. Rev. Fluid Mech. **22**(1), 539–562 (1990).
[15] C. H. K. Williamson, "Vortex dynamics in the cylinder wake," Annu. Rev. Fluid Mech. **28**(1), 477–539 (1996).
[16] A. Kumar De and A. Dalal, "Numerical simulation of unconfined flow past a triangular cylinder," Int. J. Numer. Methods Fluids **52**(7), 801–821 (2006).
[17] M. M. Koochesfahani, "Vortical patterns in the wake of an oscillating airfoil," AIAA J. **27**(9), 1200–1205 (1989).
[18] T. Schnipper, A. Andersen, and T. Bohr, "Vortex wakes of a flapping foil," J. Fluid Mech. **633**, 411–423 (2009).
[19] R. Godoy-Diana, J.-L. Aider, and J. Eduardo Wesfreid, "Transitions in the wake of a flapping foil," Phys. Rev. E **77**(1), 016308 (2008).
[20] M. Argentina and L. Mahadevan, "Fluid-flow-induced flutter of a flag," Proc. Natl. Acad. Sci. U. S. A. **102**(6), 1829–1834 (2005).
[21] B. S. H. Connell and D. K. P. Yue, "Flapping dynamics of a flag in a uniform stream," J. Fluid Mech. **581**, 33–67 (2007).
[22] M. J. Shelley and J. Zhang, "Flapping and bending bodies interacting with fluid flows," Annu. Rev. Fluid Mech. **43**, 449–465 (2011).
[23] S. Taneda, "Waving motions of flags," J. Phys. Soc. Jpn. **24**(2), 392–401 (1968).
[24] J. Zhang, S. Childress, A. Libchaber, and M. Shelley, "Flexible filaments in a flowing soap film as a model for one-dimensional flags in a two-dimensional wind," Nature **408**(6814), 835–839 (2000).
[25] S. Alben and M. J. Shelley, "Flapping states of a flag in an inviscid fluid: Bistability and the transition to chaos," Phys. Rev. Lett. **100**(7), 074301 (2008).
[26] S. Michelin, S. G. Llewellyn Smith, and B. J. Glover, "Vortex shedding model of a flapping flag," J. Fluid Mech. **617**, 1–10 (2008).
[27] J. M. Anderson, K. Streitlien, D. S. Barrett, and M. S. Triantafyllou, "Oscillating foils of high propulsive efficiency," J. Fluid Mech. **360**, 41–72 (1998).
[28] M. J. Lighthill, "Large-amplitude elongated-body theory of fish locomotion," Proc. R. Soc. London, Ser. B **179**(1055), 125–138 (1971).
[29] M. S. Triantafyllou, A. H. Techet, and F. S. Hover, "Review of experimental work in biomimetic foils," IEEE J. Oceanic Eng. **29**(3), 585–594 (2004).
[30] M. S. Triantafyllou, G. S. Triantafyllou, and D. K. P. Yue, "Hydrodynamics of fishlike swimming," Annu. Rev. Fluid Mech. **32**(1), 33–53 (2000).
[31] R. W. Davis, E. F. Moore, and L. P. Purtell, "A numerical–experimental study of confined flow around rectangular cylinders," Phys. Fluids **27**(1), 46–59 (1984).
[32] H. Suzuki, Y. Inoue, T. Nishimura, K. Fukutani, and K. Suzuki, "Unsteady flow in a channel obstructed by a square rod (crisscross motion of vortex)," Int. J. Heat Fluid Flow **14**, 2–9 (1993).
[33] S. Camarri and F. Giannetti, "On the inversion of the von Kármán street in the wake of a confined square cylinder," J. Fluid Mech. **574**, 169–178 (2007).
[34] S. Singha and K. P. Sinhamahapatra, "Flow past a circular cylinder between parallel walls at low Reynolds numbers," J. Ocean Eng. **37**, 757–769 (2010).
[35] L. Zovatto and G. Pedrizzetti, "Flow about a circular cylinder between parallel walls," J. Fluid Mech. **440**, 1–25 (2001).
[36] C. Q. Guo and M. P. Paidoussis, "Stability of rectangular plates with free side-edges in two-dimensional inviscid channel flow," J. Appl. Mech. **67**(1), 171–176 (2000).
[37] S. Alben, "Flag flutter in inviscid channel flow," Phys. Fluids **27**(3), 033603 (2015).
[38] P. Hidalgo and A. Glezer, "Direct actuation of small-scale motions for enhanced heat transfer in heated channels," in *ASME-JSME-KSME 2011 Joint Fluids Engineering Conference* (American Society of Mechanical Engineers, 2011), pp. 3123–3129.
[39] W. R. Briley, "A numerical study of laminar separation bubbles using Navier–Stokes equations," J. Fluid Mech. **47**, 713–736 (1971).

[40] M. Napolitano, G. Pascazio, and L. Quartapelle, "A review of vorticity conditions in the numerical solution of the $\zeta - \psi$ equations," Comput. Fluids **28**, 139–195 (1999).
[41] P. M. Gresho, "Incompressible fluid dynamics: Some fundamental formulation issues," Annu. Rev. Fluid Mech. **23**, 413–453 (1991).
[42] T. E. Tezduyar, J. Liou, and D. K. Ganjoo, "Incompressible flow computations based on the vorticity-stream function and velocity–pressure formulations," Comput. Struct. **35**, 445–472 (1990).
[43] A. J. Baker, *Finite Element Computational Fluid Mechanics* (Taylor and Francis US, 1983).
[44] T. E. Tezduyar and J. Liou, "On the downstream boundary conditions for the vorticity-stream function formulation of two-dimensional incompressible flow," Comput. Methods. Appl. Mech. Eng. **85**, 207–217 (1991).
[45] M. A. Ol'Shanskii and V. M. Staroverov, "On simulation of outflow boundary conditions in finite difference calculations for incompressible fluid," Int. J. Numer. Methods Fluids **33**(4), 499–534 (2000).
[46] A. K. Borah, "Computational study of streamfunction-vorticity formulation of incompressible flow and heat transfer problems," Appl. Mech. Mater. **52**, 511–516 (2011).
[47] G. Comini and M. Manzan, "Inflow and outflow boundary conditions in the finite element solution of the stream function-vorticity equations," Commun. Numer. Methods Eng. **11**, 33–40 (1995).
[48] R. L. Sani and P. M. Gresho, "Résumé and remarks on the open boundary condition minisymposium," Int. J. Numer. Methods Fluids **18**, 983–1008 (1994).
[49] D. J. Acheson, *Elementary Fluid Dynamics* (Oxford Univ. Press, 1990).
[50] R. Krasny, "Computation of vortex sheet roll-up in the Trefftz plane," J. Fluid Mech. **184**, 123–155 (1987).
[51] J. Happel and H. Brenner, in *Low Reynolds Number Hydrodynamics: With Special Applications to Particulate Media* (Springer, 1983), Vol. 1.
[52] S. Alben and M. Shelley, "Coherent locomotion as an attracting state for a free flapping body," Proc. Natl. Acad. Sci. U. S. A. **102**(32), 11163–11166 (2005).
[53] T. Von Kármán, *Aerodynamics: Selected Topics in the Light of their Historical Development* (Courier Dover Publications, 2004).
[54] F. H. Abernathy and R. E. Kronauer, "The formation of vortex streets," J. Fluid Mech. **13**(01), 1–20 (1962).
[55] E. Berger and R. Wille, "Periodic flow phenomena," Annu. Rev. Fluid Mech. **4**(1), 313–340 (1972).
[56] R. D. Blevins, *Flow-Induced Vibration* (Van Nostrand Reinhold Co., New York, 1977), p. 377.
[57] P. W. Bearman, "On vortex street wakes," J. Fluid Mech. **28**(04), 625–641 (1967).
[58] R. Peyret, in *Spectral Methods for Incompressible Viscous Flow* (Springer, 2002), Vol. 148.
[59] R. Peyret and T. Darwin Taylor, *Computational Methods for Fluid Flow* (Springer-Verlag, New York, 1985), p. 368.
[60] K. Suzuki and H. Suzuki, "Instantaneous structure and statical feature of unsteady flow in a channel obstructed by a square rod," Int. J. Heat Fluid Flow **15**, 426–437 (1994).
[61] P. Hidalgo, F. Herrault, A. Glezer, M. Allen, S. Kaslusky, and B. St. Rock, "Heat transfer enhancement in high-power heat sinks using active reed technology," in *Thermal Investigations of ICs and Systems (THERMINIC), 2010 16th International Workshop on* (IEEE, 2010), pp. 1–6.
[62] K. Shoele and R. Mittal, "Computational study of flow-induced vibration of a reed in a channel and effect on convective heat transfer," Phys. Fluids **26**(12), 127103 (2014).
[63] Y. Saad and M. H. Schultz, "GMRES: A generalized minimal residual algorithm for solving nonsymmetric linear systems," SIAM J. Sci. Stat. Comput. **7**(3), 856–869 (1986).
[64] S. Alben, "An implicit method for coupled flow–body dynamics," J. Comput. Phys. **227**(10), 4912–4933 (2008).